

An artificial neural network (ANN)-based lung-tumor motion predictor for intrafractional MR tumor tracking

Jihyun Yun

Department of Physics, University of Alberta, 11322-89 Avenue, Edmonton, Alberta T6G 2G7, Canada and Department of Oncology, Medical Physics Division, University of Alberta, 11560 University Avenue, Edmonton, Alberta T6G 1Z2, Canada

Marc Mackenzie, Satyapal Rathee, and Don Robinson

Department of Medical Physics, Cross Cancer Institute, 11560 University Avenue, Edmonton, Alberta T6G 1Z2, Canada and Department of Oncology, Medical Physics Division, University of Alberta, 11560 University Avenue, Edmonton, Alberta T6G 1Z2, Canada

B. G. Fallone^{a)}

Department of Physics, University of Alberta, 11322-89 Avenue, Edmonton, Alberta T6G 2G7, Canada; Department of Medical Physics, Cross Cancer Institute, 11560 University Avenue, Edmonton, Alberta T6G 1Z2, Canada; and Department of Oncology, Medical Physics Division, University of Alberta, 11560 University Avenue, Edmonton, Alberta T6G 1Z2, Canada

(Received 16 March 2012; revised 14 May 2012; accepted for publication 6 June 2012; published 28 June 2012)

Purpose: To address practical issues of implementing artificial neural networks (ANN) for lung-tumor motion prediction in MRI-based intrafractional lung-tumor tracking.

Methods: A feedforward four-layered ANN structure is used to predict future tumor positions. A back-propagation algorithm is used for ANN learning. Adaptive learning is incorporated by continuously updating weights and learning rate during prediction. An ANN training scheme specific for MRI-based tracking is developed. A multiple-ANN structure is developed to reduce tracking failures caused by the lower imaging rates of MRI. We used particle swarm optimization to optimize the ANN structure and initial weights (IW) for each patient and treatment fraction. Prediction accuracy is evaluated using the 1D superior–inferior lung-tumor motions of 29 lung cancer patients for system delays of 120–520 ms, in increments of 80 ms. The result is compared with four different scenarios: (1), (2) ANN structure optimization + with/without IW optimization, and (3), (4) no ANN structure optimization + with/without IW optimization, respectively. An additional simulation is performed to assess the value of optimizing the ANN structure for each treatment fraction.

Results: For 120–520 ms system delays, mean RMSE values (ranges 0.0–2.8 mm from 29 patients) of 0.5–0.9 mm are observed, respectively. Using patient specific ANN structures, a 30%–60% decrease in mean RMSE values is observed as a result of IW optimization, alone. No significant advantages in prediction performance are observed, however, by optimizing for each fraction.

Conclusions: A new ANN-based lung-tumor motion predictor is developed for MRI-based intrafractional tumor tracking. The prediction accuracy of our predictor is evaluated using a realistic simulated MR imaging rate and system delays. For 120–520 ms system delays, mean RMSE values of 0.5–0.9 mm (ranges 0.0–2.8 mm from 29 patients) are achieved. Further, the advantage of patient specific ANN structure and IW in lung-tumor motion prediction is demonstrated by a 30%–60% decrease in mean RMSE values. © 2012 American Association of Physicists in Medicine. [<http://dx.doi.org/10.1118/1.4730294>]

Key words: motion prediction, intrafraction motion management, lung-tumor tracking, linac-MR, MRI guidance

I. INTRODUCTION

To ensure improved targeting and delivery of highly conformal radiation dose to mobile tumors, several groups are actively researching intrafractional tumor tracking systems.^{1–3} Lung-tumors are of special interest for tracking, due to their potential for large ranges of motion during treatment delivery. Studies have shown that lung-tumors may move up to 50 mm in superior–inferior (SI) direction, 15 mm in anterior–posterior (AP), and 10 mm in left–right (LR) direction during normal breathing.^{4,5}

Krauss *et al.*⁶ and Sawant *et al.*² performed phantom studies demonstrating the feasibility of 2D intrafractional lung-tumor tracking using a Siemens 160 leaf multileaf collimator (MLC) and a Varian 120 leaf MLC, respectively. In both studies, a tumor surrogate was driven according to a sinusoidal trajectory and its position was detected via a motion monitoring system developed by Calypso Medical Technologies (Seattle, WA). Cho *et al.* suggested the simultaneous use of kV/MV imaging for 3D intrafractional tracking, where a gold marker was used as a tumor surrogate.³ Recently, Cervino *et al.* conducted a feasibility

study in regard to MRI-guided lung-tumor tracking by following healthy volunteers' lung vascular structures in cine-MR images.⁷ Our group at the Cross Cancer Institute has been developing a MRI-based intrafractional lung-tumor tracking system by taking advantage of the intrafractional MR imaging feature of the linac-MR that is installed in our laboratory.^{8–10}

Although tracking mechanisms may vary, the use of on-line MLC controlling technique (i.e., not preprogrammed leaf motions) for intrafractional beam conformation is fairly common.^{2,3,6} Ideally, intrafractional tracking would provide target detection and beam delivery simultaneously. However, there exists an inevitable system delay between the two events due to (1) the time requirement to drive each leaf of the MLC to its designated position and (2) computing/processing time. Previously reported system delays range from 160 to 500 ms (Refs. 2, 3, and 6) depending on tracking method. In the case of a lung-tumor whose motion-speed is known to be in the range of 4–94 mm/s,¹¹ a system delay of 500 ms could lead tumor localization errors of up to a maximum of 47 mm. In the presence of this inevitable system delay, a method of predicting tumor motion is highly desirable in order to reduce the localization errors.

Various prediction algorithms have been proposed to compensate for tumor motion during system delay.^{12–14} Due to the highly nonlinear nature of lung-tumor motions which show variable speed and period, several groups have investigated the use of artificial neural networks (ANN) for motion prediction.^{15,16} Although these studies show promising results, the following issues must be addressed to implement ANN in lung-tumor motion prediction for MRI-based tumor tracking.

First, the performance of an ANN is known to be strongly dependent on its structure and initial weights (IW).^{17,18} As Verma *et al.* stated,¹⁴ ANN architecture must be optimized to be used in tumor motion prediction. However, no previous study regarding lung-tumor motion prediction has investigated this issue.

Second, previous studies assume the tumor position detection at 30 Hz by monitoring the position of external or internal tumor surrogates using optical tracking devices,^{15,16} or a stereoscopic x-ray fluoroscopy system.^{12,13} However, dynamic MR imaging to observe organ motion of lung,⁷ intrathoracic tumor,¹⁹ joint,²⁰ etc., can typically achieve image-acquisition rates of 3–4 frames per second (fps). This rate is recommended for real-time tracking of lung-tumor motion²¹ and can be achieved using our present linac-MR. Nevertheless, no previous study has been developed and evaluated for predicting lung-tumor motion using MRI-based tumor tracking.

To overcome these issues, we propose an ANN-based lung-tumor motion predictor for MRI-based intrafractional lung-tumor tracking. This report describes the ANN design and training methods, implementation of multiple-ANNs, and optimization schemes of ANN structure and IW. The prediction accuracy of our predictor is evaluated using data from 29 lung cancer patients with various possible system delays.

II. MATERIALS AND METHODS

II.A. Overview of lung-tumor motion prediction

The development of our predictor involves the following points and assumptions: (1) the position of a tumor may be represented by its centroid, (2) the position of tumor centroid in each MR image is automatically detected in real-time (less than 5 ms) using our autocontouring algorithm,⁹ (3) signal acquisition time for each MR image is 280 ms, and (4) the amount of system delay, i.e., the time interval between the detection of current tumor position and the beam delivery, of a given tracking system is known.

In our present linac-MR, system delay is ~ 200 ms, which is the sum of: (1) one half of the acquisition time, 140 ms, contributes to system delay assuming the acquired image detects the tumor position at the midpoint of k-space, (2) ~ 35 ms for image reconstruction and processing, and (3) ~ 25 ms for MLC motion.

An overview of the prediction procedure for lung-tumor motion is described in Fig. 1. In Step 1 of Fig. 1, an ANN structure and IW are optimized prior to actual treatment for each patient. A patient typically undergoes treatment over multiple fractions, where, presumably tumor motions in two consecutive fractions are the most similar. During optimization, tumor motion data recorded from a previous fraction is used as a training pattern. We used 8 min length of 1D SI lung-tumor motion pattern. More details regarding training patterns follow in Sec. II.B.

One epoch refers to a single passing of a training pattern (prediction followed by weights corrections) through the ANN during iterative trainings. In Step 2, the optimized ANN structure and IW are further trained for 900 epochs immediately prior to the actual treatment. The training set will be tumor motions recorded from 2 min of MR scan immediately prior to the treatment. In our computer platform, ~ 30 s are required to run 900 epochs.

All algorithms are coded in LabVIEW 2011 (National Instruments, Austin, TX) and tested on a 32-bit computer system (Windows7, Intel i7-2600k, 4 GB RAM).

II.B. Patient lung-tumor motion data

Our algorithm was verified using data previously reported by Suh *et al.*,²² who analyzed thoracic and abdominal

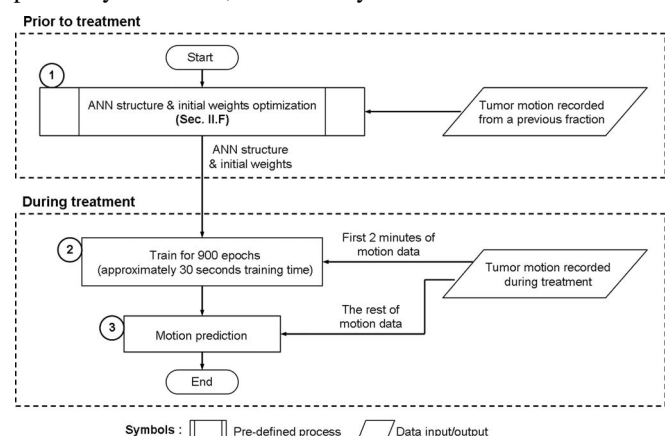


FIG. 1. Flowchart for overall lung-tumor motion prediction.

tumor motions obtained with a Cyberknife Synchrony treatment system (Accuray Incorporated, Sunnyvale, CA). During radiation treatment, 3D tumor positions were estimated and recorded every 40 ms (25 Hz) by both internal and external fiducials for various tumor sites such as lung, liver, pancreas, retroperitoneum, etc. We selected the data from the 29 lung-tumor patients. Each patient's data consists of lung-tumor motions recorded from three consecutive fractions (1–5 days apart). From each fraction, we used 8 min of the 1D SI lung-tumor motion pattern.

II.C. ANN for lung-tumor motion prediction

II.C.1. ANN structure

A feedforward four-layered ANN structure (one input layer, two hidden layers, and one output layer) is developed as shown in Fig. 2. Input and hidden layers have an additional bias input of +1, which prevents a zero output when all input values are zero. Detailed explanations can be found in Haykin.²³ Current and previous tumor positions are input to the ANN, which outputs a future tumor position. The number of hidden layers can vary, either one or two, and is determined by ANN structure optimization as explained in Sec. II.F.1.a.

$$\eta = \mu \cdot \frac{\|e_{H1}\|^2}{\|\bar{J} \cdot e_{H1}\|^2 + \gamma} = \mu \cdot \frac{(e_{H1})^2}{\sum_{k=1}^m \sum_{c=0}^n (\delta_{Fk} \cdot x(t - c \cdot \tau))^2 + \sum_{p=1}^s \sum_{q=1}^{m+1} (\delta_{Gp} \cdot Y_{fq})^2 + \sum_{i=1}^{s+1} (\delta_{H1} \cdot Y_{gi})^2 + \gamma}, \quad (4)$$

where, $\bar{J} = \partial(\text{ANN output})/\partial \bar{w}$, μ : scaling factor, γ : small constant to prevent numerical instability of η when e_{H1} is near zero. The values of μ and γ are determined to achieve the lowest prediction error using training patterns, and the results are stated in Figs. 5 and 6.

Adaptive learning is incorporated by continuously updating the weights and η of a given ANN during motion prediction. The structure of ANN does not change during prediction. However, the weights and η updates occur prior to each prediction immediately following current tumor position detection by the tracking system. This update involves simple matrix calculations that happen almost instantaneously using our computer system; thus, this is not included in calculating the total system delay.

In this way, the ANN's learning process is not limited to the training sessions alone but continues during the actual tracking session. Using this ANN, our predictor can adapt quickly to tumor motion pattern during the actual tracking session, even when this pattern starts deviating from the one used in training sessions.

II.D. ANN training for MRI-based tumor tracking

Our tumor motion training data are acquired at 280 ms intervals from MR images obtained from previous treatment

II.C.2. Back-propagation algorithm and adaptive learning

We used a back-propagation (BP) algorithm²³ for ANN learning, i.e., updating weights. Following the same notations as in Fig. 2, we used the following Eqs. (1)–(3) to update weights during training

$$W_{\text{new}} = W_{\text{previous}} + \Delta W, \quad (1)$$

where, w_{new} : new weight, w_{previous} : previous weight, Δw : weight update.

For weights associated with output neuron,

$$\Delta w_{g \rightarrow h}^{a1} = \eta \cdot \delta_{H1} \cdot Y_{ga}, \quad (2)$$

where, η : learning rate, $\delta_{H1} = e_{H1} \cdot \Phi'(V_{h1})$, e_{H1} = desired output—ANN output, and $\Phi'(V_{h1}) = d\Phi/dV_{h1} = \Phi(V_{h1}) \cdot (1 - \Phi(V_{h1}))$.

For weights associated with other neurons,

$$\Delta w_{f \rightarrow g}^{ab} = \eta \cdot \delta_{Gb} \cdot Y_{fa}, \quad (3)$$

where, $\delta_{Gb} = \Phi'(V_{Gb}) \cdot \sum_{a=1}^{s+1} (\delta_{H1} \cdot w_{g \rightarrow h}^{a1})$.

The BP algorithm requires a proper learning rate (η) to achieve fast convergence. We implemented an algorithm developed by Behera *et al.*,²⁴ which can calculate an efficient, self-adaptive learning rate as

fractions. In reality, the system delay will often be different from the time intervals in the training data. To demonstrate that this training scheme can be applied to different system delays, we present ANN training simulations with 280 and 200 ms system delays. Figure 3 shows a portion of the training data from one of the 29 patients.

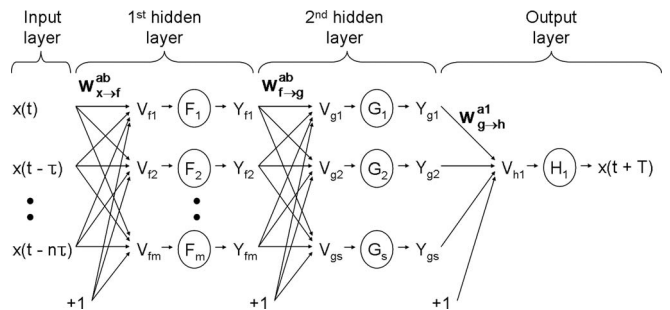


FIG. 2. A feedforward four-layered ANN structure. $x(t)$: position of tumor at time t , τ : time interval between tumor position updates, T : system delay of a given tracking system, V_{cd} : input to d^{th} activation function of layer “ c ” (i.e., $V_{gb} = \sum_{a=1}^{m+1} w_{f \rightarrow g}^{ab} \cdot Y_{fa}$), F, G, H : activation function $\Phi(x) = 1/(1 + \exp(-x))$, x can be $V_{f1, f2, \dots, fm}$, $V_{g1, g2, \dots, gs}$, or V_{h1} , Y_{cd} : output from d^{th} activation function of layer “ c ” (e.g., $Y_{f1} = \Phi(V_{f1})$), $w_{f \rightarrow g}^{ab}$: weight associated with the output of a^{th} neuron in f layer to b^{th} neuron in g layer, $x(t+T)$: ANN output (predicted tumor position).

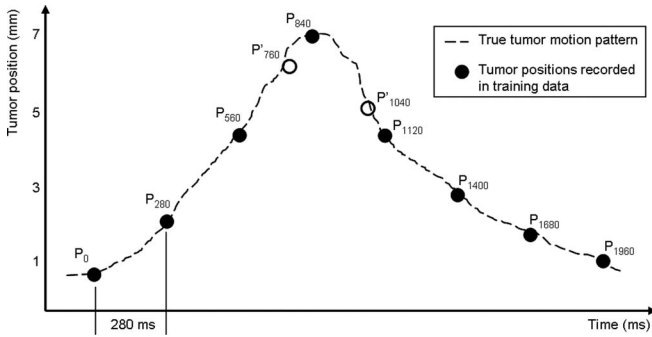


FIG. 3. Tumor position in S–I direction in training data, P_t : tumor position at time t (ms), P'_t : approximate tumor position at t (ms).

During ANN training, many numbers of known input/output pairs must be entered to allow the ANN to model the complex relationships between them. These input/output pairs include the previous, as well as future, tumor positions that have been recorded in the training data.

As shown in Fig. 2, a single ANN can predict a single output for tumor position. However, the number of inputs to this ANN, i.e., number of previous tumor positions, can vary from patient to patient. Section II.F explains how our predictor determines the appropriate number of inputs for each patient. Here, our training scheme takes three inputs and is described in the following two examples.

- (1) 280 ms system delay: Input/output pairs were generated from the training data described above with a system delay of 280 ms. In Fig. 3, P_0 , P_{280} , P_{560} can be used as the ANN inputs of the 1st input/output pair. In this case, the output should be P_{840} , because the time interval between P_{560} and P_{840} is the same amount as the system delay. Similarly, if P_{280} , P_{560} , P_{840} are used as the inputs for the 2nd input/output pair, P_{1120} will be the corresponding output. We can generate many numbers of input/output pairs in this way and train the ANN. The same training method can be used if the system delay is an exact multiple of the time interval between two consecutively known tumor positions in training data.
- (2) 200 ms system delay: Because the system delay for our present linac-MR system is 200 ms, a different method is used to generate the input/output pairs. If P_0 , P_{280} , P_{560} are used as the inputs, the output must be P_{760} . However, P_{760} is unknown in our training data as shown in Fig. 3. Our approach is to approximate P_{760} using linear interpolation between P_{560} and P_{840} , which is referred as P'_{760} . This is a first order approximation which presumes that the lung-tumor motion may be reasonably modeled as linear motion between two known tumor positions. Similarly, if P_{280} , P_{560} , P_{840} are used as the inputs, P'_{1040} will be the corresponding output. Using this method, we are able to train our ANN for any arbitrary system delay.

II.E. Implementation of multiple ANNs

During tumor tracking, each prediction occurs immediately after a current tumor position is detected. This triggers MLC motion to conform the radiation beam to the tumor at the predicted position.

Frequent tracking failures may occur if a single ANN is used in our predictor. If the time interval between two predictions is greater than the time required to complete the MLC motion, the MLC will stop after reaching set points, i.e., designated leaf positions, and wait for the next prediction to occur. During this time, designated as the “MLC-off time,” the tumor will continue to move resulting in tracking failure. On the contrary, if the time interval between two predictions is smaller than the time required for the MLC to reach the predicted position, then the MLC will never reach the set points and miss the tumor.

We propose to employ multiple ANNs in our predictor to reduce tracking failures, which, in itself, is a unique feature developed in this study.

II.E.1. Tumor tracking using multiple ANNs

We use seven ANNs, because our imaging rate is 280 ms and we want to predict tumor positions in a 40 ms interval that corresponds to the acquisition rate of the Suh *et al.*²² data used to evaluate the performance of the prediction algorithm (the acquisition rate of the Suh *et al.* data is 40 ms, and 280/40 is 7).

The seven ANNs implemented in our predictor have an identical structure. However, we trained them separately so that at each prediction, the predictor can output seven consecutive future tumor positions (40 ms apart, the first one corresponds to the future tumor position after the system delay). In case of 200 ms system delay, the 1st ANN predicts a tumor positions at 200 ms in the future, 2nd ANN predicts at 240 ms in the future, 3rd ANN predicts at 280 ms in the future, etc. This is described in Fig. 4.

At 0 ms, the 1st prediction occurs from seven ANNs predicting P_{200} , P_{240} , ..., P_{440} . Using these, the MLC controller triggers MLC motions conforming to the appropriate future tumor positions. For example, at 0 ms, the MLC begins conforming to P_{200} ; at 40 ms, it starts conforming to P_{240} , etc. At 280 ms, the 2nd prediction occurs predicting P_{480} , P_{520} , ..., P_{720} , and this triggers new MLC motions.

Using multiple ANNs, we can trigger MLC motions more frequently. We can then verify whether this approach will reduce tracking failures because (1) the MLC-off time between two predictions is decreased, and (2) the MLC can almost

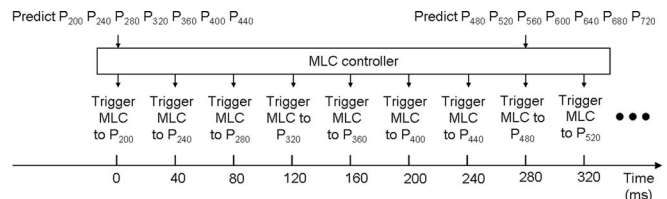


FIG. 4. Tumor tracking using seven ANNs, P_t : tumor position at time t (ms).

always reach the set points, since the traveling distance at each motion triggering is decreased.

II.F. Optimizing ANN structure and IW for each patient

ANN structure and IW must be optimized for each patient to ensure the optimal performance of our predictor, because (1) the performance of ANN is known to be strongly dependent on its structure and IW,^{17,18} and (2) there are large patient-to-patient variations in lung-tumor motion patterns.

II.F.1. Particle swarm optimization

Particle swarm optimization (PSO) is one type of population-based stochastic optimization method, which is inspired by the social behavior of bird flocking or fish schooling.²⁵ PSO optimization begins by generating a number of candidate solutions called “particles” that are spread over an *n*-dimensional solution space with different positions and velocities. Each particle’s current position represents a current solution to a given optimization problem, and its velocity represents the modification of current solution toward a new, more optimized solution. These particles will “fly” through the solution space, in order to find a specific location where the solution at that location will produce the optimum result with regard to a user defined fitness function.

We use an improved version of the original PSO algorithm called modified particle swarm optimization (MPSO) (Ref. 26) for both ANN structure and IW optimizations. Shi *et al.* demonstrated superior performance of MPSO in finding a global optimum within a reasonable number of iterations.²⁶ This is particularly advantageous in clinical applications where optimization for each patient must be completed within a reasonable time frame.

In MPSO, each particle’s velocity and position are updated in each iteration as

$$V_{\text{updated}} = W \cdot V_{\text{prev}} + c_1 \cdot \text{rand}_1 \cdot (pbest - P_{\text{prev}}) + c_2 \cdot \text{rand}_2 \cdot (gbest - P_{\text{prev}}), \tag{5}$$

$$P_{\text{updated}} = P_{\text{prev}} + V_{\text{updated}}, \tag{6}$$

where, V_{updated} , P_{updated} : updated velocity and position of a particle, W : inertia weight, c_n : a unitless weight determining the impact of an individual particle’s history on the entire swarm’s history in V_{updated} calculation, rand_n : a random number (0–1), $pbest$: personal best solution, $gbest$: global best solution, V_{prev} , P_{prev} : previous velocity and position of a particle. Detailed calculation methods of $pbest$ and $gbest$ follow in Sec. II.F.1.a.

We use MPSO to optimize ANN structure and IW for each patient. To achieve this, we must first determine the representation of a particle and a fitness function for each optimization problem. Detailed explanations follow.

II.F.1.a. ANN structure optimization. In ANN structure optimization, a specific ANN structure is a solution, i.e., particle. Therefore, each particle’s current position and velocity represents a current ANN structure and the degree of its mod-

ification, respectively. Our fitness function is a RMSE value between original and predicted tumor positions in the training pattern, where original tumor positions refer to the ones recorded in patient data.

As shown in Fig. 2, we can define an ANN structure using an array of three integer variables designating the number of inputs, number of neurons in 1st hidden layer, and number of neurons in 2nd hidden layer. The number of neurons in an output layer is fixed at 1.

For example, $[n, m, s]$ indicates an ANN structure that has *n* number of inputs, *m* number of neurons in the 1st hidden layer, *s* number of neurons in the 2nd hidden layer, and 1 neuron in the output layer. Hence, each particle’s position and velocity are both defined by a 1×3 integer array. Figure 5 shows the ANN structure optimization process.

Step 1 is performed only in the 1st iteration at $M = 1$. Here, the position and velocity arrays of ten particles are generated using a random number generator within a user defined range as stated in Fig. 5. In Step 2, each particle’s velocity array is recorded for later use.

In Step 3, the N^{th} particle’s position array is read and its corresponding ANN is created. In Step 4, this ANN is copied

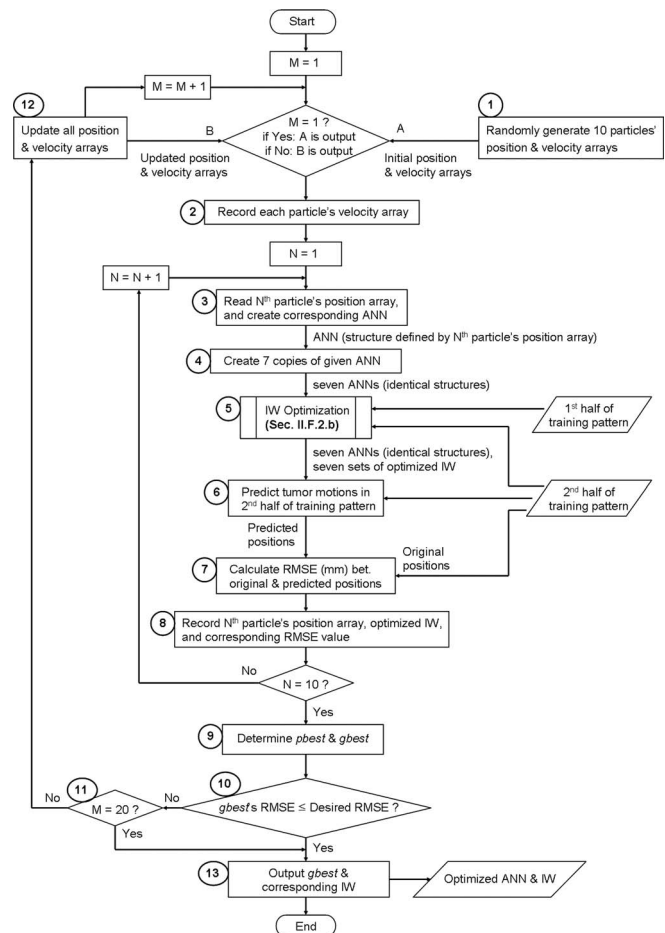


FIG. 5. Flow chart for ANN structure optimization. Parameters used: Step 1 (initial number of inputs: 1–10, initial number of neurons in each layer: 0–10, initial velocity: 0–10), Step 6 [μ : 0.6, γ : 0.02, see Eq. (4)], Step 10 (desired RMSE = 0.001 mm), Step 12 [$c_n = 2$, rand_n : 0–1, max. velocity: 10, W : 0.4, see Eq. (5)].

seven times to create seven ANNs that have identical structures. For example, if the 1st particle's position array is [5, 8, 6], the corresponding ANN is created containing 5 inputs, 8 and 6 neurons in the 1st and 2nd hidden layers, and 1 output neuron. This ANN is then copied seven times.

In Step 5, IW are optimized for each of the seven ANNs using the 1st half of the training pattern. During IW optimization, each ANN is trained for a different amount of system delay. Detailed explanations follow in Sec. II.F.1.b. As a result, seven sets of optimized IW are produced.

In Step 6, the seven ANNs and a corresponding set of optimized IW are used to predict tumor motions in the 2nd half of the training pattern. This generates predicted tumor positions in 40 ms intervals as explained in Sec. II.E.1. Using this result, in Step 7, we can perform one-to-one comparisons between original and predicted tumor positions calculating RMSE values.

Steps 3–7 are iterated with all ten particles' position arrays. After the N^{th} iteration, the N^{th} particle's position array, optimized IW, and corresponding RMSE value are recorded in Step 8. From this record, the algorithm determines $pbest$ and $gbest$ in Step 9 as described in the following paragraphs.

During optimization, each particle's position array is updated through iterations. Out of the particle's current and previous position arrays, $pbest$ is the one that achieved the lowest RMSE value in Step 7. For example, if the 1st particle's position array has been updated for three iterations (see the outer loop through Step 12) as [5, 8, 6] \rightarrow [10, 18, 7] \rightarrow [12, 23, 0] with corresponding RMSE values of 2.5 \rightarrow 1.6 \rightarrow 1.9, then $pbest$ of this particle is [10, 18, 7].

In Step 9, therefore, ten $pbest$ arrays are determined from ten particles. Out of these, the one with the lowest RMSE value becomes $gbest$. Depending on the results from Steps 10 and 11, the algorithm either updates all particles' position arrays and iteration continues, or the optimization process is terminated.

In Step 12, we first calculate V_{updated} array for each particle using Eq. (5) with the parameters stated in Fig. 5. Each particle's velocity, position, and $pbest$ arrays are obtained from Steps 2, 8, and 9, respectively. $gbest$ is obtained from Step 9.

For example, if the 1st particle's position, velocity, $pbest$ arrays are $[P_1, P_2, P_3]$, $[V_1, V_2, V_3]$, $[PB_1, PB_2, PB_3]$, respectively, and $gbest$ of all particles is $[GB_1, GB_2, GB_3]$, then V_{updated} is calculated as

$$\begin{aligned} V_{\text{updated array}} &= [V_{\text{updated1}}, V_{\text{updated2}}, V_{\text{updated3}}] \\ &= W \cdot [V_1, V_2, V_3] + c_1 \cdot \text{rand}_1 \cdot ([PB_1, PB_2, PB_3] - [P_1, P_2, P_3]) \\ &\quad + c_2 \cdot \text{rand}_2 \cdot ([GB_1, GB_2, GB_3] - [P_1, P_2, P_3]). \end{aligned}$$

Hence,

$$\begin{aligned} V_{\text{updated1}} &= W \cdot V_1 + c_1 \cdot \text{rand}_1 \cdot (PB_1 - P_1) + c_2 \cdot \text{rand}_2 \cdot (GB_1 - P_1), \\ V_{\text{updated2}} &= W \cdot V_2 + c_1 \cdot \text{rand}_1 \cdot (PB_2 - P_2) + c_2 \cdot \text{rand}_2 \cdot (GB_2 - P_2), \\ V_{\text{updated3}} &= W \cdot V_3 + c_1 \cdot \text{rand}_1 \cdot (PB_3 - P_3) + c_2 \cdot \text{rand}_2 \cdot (GB_3 - P_3). \end{aligned}$$

If any component of the V_{updated} array is greater than a user defined maximum velocity stated in Fig. 5, that component is replaced with the value of maximum velocity. This is to avoid overly radical changes of the particle's position in each iteration. After the V_{updated} array is determined, P_{updated} array is calculated using Eq. (6) as

$$\begin{aligned} P_{\text{updated array}} &= [P_{\text{updated1}}, P_{\text{updated2}}, P_{\text{updated3}}] \\ &= [P_1, P_2, P_3] + [V_{\text{updated1}}, V_{\text{updated2}}, V_{\text{updated3}}]. \end{aligned}$$

Hence,

$$\begin{aligned} P_{\text{updated1}} &= P_1 + V_{\text{updated1}}, \quad P_{\text{updated2}} = P_2 + V_{\text{updated2}}, \\ P_{\text{updated3}} &= P_3 + V_{\text{updated3}}. \end{aligned}$$

Steps 2–11 are iterated after all ten particles' position and velocity arrays are updated. At the end of optimization in Step 13, the algorithm outputs an ANN structure and IW optimized for a given patient.

II.F.1.b. IW optimization (Step 5 in Fig. 5). The weights shown in Fig. 2 are rational numbers, and one may calculate the number of weights required to link two adjacent layers as: (number of neurons in previous layer + 1) \times number of neurons in next layer, where the + 1 term is due to the bias input. For example, if a $[n, m, s]$ structure is given, the total number of IW, referred as Z , is calculated as: $Z = (n + 1) \times m + (m + 1) \times s + (s + 1) \times 1$. Hence, one set of IW for a $[n, m, s]$ structure is defined by a $1 \times Z$ rational number array.

We have seven ANNs in our predictor, which must be trained for different amounts of system delay. Therefore, a group of IW becomes a solution, i.e., particle, in IW optimization, where this group consists of seven sets of IW. Each particle's current position and velocity represents a current group of IW and the degree of its modification, respectively. Since a group of IW contains seven sets of IW, each particle's position and velocity are both defined by seven $1 \times Z$ rational number arrays. The same fitness function is used as in ANN

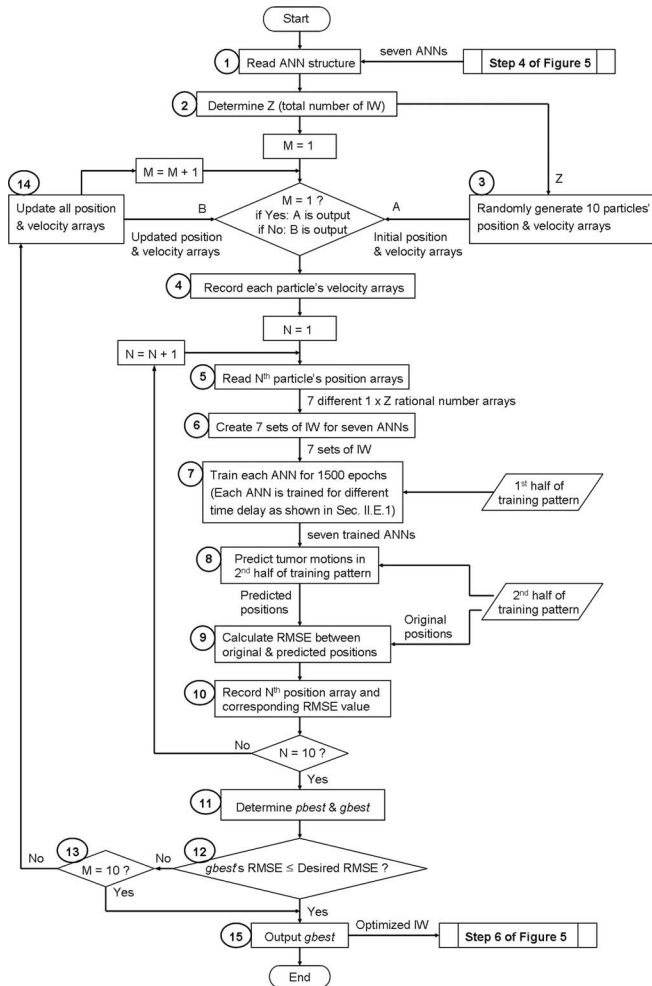


FIG. 6. Flow chart for IW optimization. Parameters used: Step 3 (IW and initial velocities: random rational numbers bet. -1 and 1), Steps 7, 8 (μ : 0.6 , γ : 0.02), Step 12 (Desired RMSE = 0.001 mm), Step 14 ($c_n = 2$, $rand_n$: $0-1$, Max. velocity/W: $1.5/0.8$ and $2/0.6$ for one and two hidden-layered ANN, respectively).

structure optimization. Figure 6 shows the IW optimization processes.

In Steps 1 and 2, we read the ANN structure subject to IW optimization and calculate Z . For example, if the ANN has a $[5, 8, 6]$ structure, $Z = (5 + 1) \times 8 + (8 + 1) \times 6 + (6 + 1) \times 1 = 109$. Because the seven ANNs have identical structures, we only need a single Z value.

Step 3 is performed only in the 1st iteration at $M = 1$. We generate ten particles' position and velocity arrays using a random number generator between -1 and 1 . In Step 4, each particle's velocity arrays are recorded for later use.

In Steps 5 and 6, the N^{th} particle's position arrays are read and corresponding sets of IW are created. As a result, seven sets of IW are created for the seven ANNs.

In Step 7, the seven ANNs are trained using the 1st half of training pattern. Each ANN is trained for a different amount of system delay for 1500 epochs. The 1st, 2nd, ..., 7th sets of IW are used as a starting point for training the 1st, 2nd, ..., 7th ANNs, respectively.

In Step 8, we use the seven trained ANNs to predict tumor motions in the 2nd half of training pattern. This generates predicted tumor positions in 40 ms intervals as explained in Sec. II.E.1. Hence, in Step 9, we can calculate RMSE between the original and predicted tumor positions to evaluate the prediction accuracy.

Steps 5–9 are iterated with all ten particles' position arrays. After the N^{th} iteration, the N^{th} particle's position arrays and corresponding RMSE value are recorded in Step 10. From this record, the algorithm determines $pbest$ and $gbest$ in Step 11. This process is previously explained in Sec. II.F.1.a in detail. Depending on the results from Steps 12 and 13, the algorithm either updates all particles' position arrays and iteration continues, or the optimization process is terminated.

In Step 14, V_{updated} and P_{updated} arrays are calculated for each particle using Eqs. (5) and (6) with the parameters stated in Fig. 6. Detailed explanations have been previously given in Sec. II.F.1.a. After all particles' position and velocity arrays are updated, Steps 4–13 continue using the updated arrays. At the end of optimization in Step 15, the algorithm outputs the seven sets of IW represented by $gbest$ as the optimized IW.

II.G. Evaluation of the reduction in tracking failures using multiple ANNs

We verified whether using multiple ANN reduces tracking failures as described in Sec. II.E. Lung-tumor tracking was simulated using a Varian 52-leaf MLC, where tumor motion was assumed to be sinusoidal (period: 4 s, amplitude: 5 cm) at the imaging plane of our present linac-MR. This tumor motion is sufficient to cover the possible motion range of lung-tumors.^{4,5}

The following two cases were tested during 1 min of tumor tracking:

- (1) MLC motions were triggered every 280 ms, which will occur if a single ANN is used;
- (2) MLC motions were triggered every 40 ms, which will occur if seven ANNs are used.

In both cases, mean and standard deviation of the MLC-off time, and the percentage frequency of MLC failure to reach set points were calculated.

II.H. Evaluation of prediction accuracy using patient data

II.H.1. Presentation of patient data to ANNs

To evaluate the prediction accuracy of our predictor in a realistic MRI-based tumor tracking scenario, the following processes are performed with the original data from Suh et al.²²

First, to simulate MRI-based tumor tracking that detects tumor positions every 280 ms, every 7th data point is chosen from the original data (40 ms interval between data points $\times 7 = 280$ ms). This generates motion patterns containing lung-tumor positions recorded every 280 ms. Second, each motion pattern is shifted and normalized, so that the values remain between 0 and 1. This is clinically feasible, and more details

TABLE I. Four cases tested for prediction accuracy investigation.

| | Case 1 | Case 2 | Case 3 | Case 4 |
|----------------------------|--------|--------|--------|--------|
| ANN structure optimization | Yes | Yes | No | No |
| IW optimization | Yes | No | Yes | No |

follow in Sec. IV. It is important to note that only these motion patterns are presented to our predictor, both in ANN training and the motion prediction stages.

II.H.2. Prediction accuracy comparisons

The prediction accuracy of our predictor is evaluated with 29 patient data sets. Each patient's 1st fraction data is used as a training pattern for the ANN structure and IW optimizations. The result is used to predict tumor motions in the 2nd fraction data. Similarly, 2nd fraction data are used as a training pattern for optimizations, and this result is used to predict tumor motions in the 3rd fraction data.

Evaluation is performed for various amounts of system delay ranging from 120 to 520 ms in 80 ms increments, which encompasses all previously reported system delays in the literature.^{2,3,6} Prediction accuracy is measured by the RMSE (mm) between original and predicted tumor positions.

To demonstrate the benefit of ANN structure as well as IW optimizations developed in this study, prediction accuracy was compared according to the four different cases shown in Table I.

Instead of using an optimized ANN structure for each patient, a single ANN structure (25 inputs, 2 neurons in a hidden layer, 1 output neuron) is employed for all patients in cases 3 and 4. This ANN structure was suggested by Murphy *et al.*¹⁶ for respiratory motion prediction, which is closely correlated to abdominal tumor motions including lung-tumor.²⁷ The IW optimization process is omitted for cases 2 and 4. However, an additional 900 epochs training as described in Step 2 of Fig. 1 is still performed with randomly generated IW.

One further experiment is performed to assess the necessity of ANN structure optimization not only for each patient but also for each treatment fraction. In this case, only 1st fraction data are used as a training pattern for ANN structure and IW optimizations, and the result is used to predict tumor motions in both 2nd and 3rd fraction data. Prediction accuracy of 3rd fraction data obtained from this experiment is compared to the result from case 1, in which the prediction was performed with an ANN structure specifically optimized to predict tumor motion in 3rd fraction data.

III. RESULTS

III.A. Tracking failure comparisons using a single ANN vs seven ANNs

Table II compares the MLC-off time between two consecutive predictions and the frequency percentage of MLC fail-

TABLE II. Tracking failure comparisons using a single ANN vs seven ANNs.

| | Single ANN | Seven ANNs |
|------------------------------|-----------------|---------------|
| MLC motion triggering | Every 280 ms | Every 40 ms |
| MLC-off time(mean \pm std) | 110 \pm 87 ms | 15 \pm 9 ms |
| Failure to reach set points | 46% | 0% |

ures reaching its set points during 1 min of tracking period. Set points are the aimed location of each leaf, and the failures result from MLC speed limitation.

In the single ANN case, mean MLC-off times show that tumor tracking failed for 110 ms on average between two consecutive MLC triggers. More importantly, the MLC could not reach its set points in 46% of the overall tracking period. Both of these problems are largely resolved using the seven ANNs approach. In this case, the MLC was always able to reach its set points, and the mean MLC-off time was decreased by a factor of more than 7.

III.B. Prediction performance using optimized ANN and IW

Table III shows lung-tumor motion prediction results simulated from patient data as discussed in Sec. II.H.1. Prediction is performed with optimized ANN structures and optimized IW for each patient and fraction. Optimizations and predictions were repeated five times for each patient and fraction. Only mean RMSE values are reported in Table III as very small variations in RMSE values (less than 0.1 mm) were observed for the five trials.

For 120–520 ms system delays, 0.5–0.9 mm of mean RMSE values (ranges 0.0–2.8 mm from 29 patients) are observed, respectively. The entire optimization process (ANN structure and IW optimizations) requires \sim 2.5 h for each treatment fraction of a given patient, which would need to be performed prior to treatment.

III.C. Prediction accuracy comparisons

Table IV compares prediction accuracies of the four different cases defined in Table I. Relative mean RMSE values for the 29 patients are calculated with respect to the largest mean RMSE values for each system delay and fraction. The largest mean RMSE values are obtained from case 4, where no optimization is performed.

By comparing the results between cases 1 and 4, a 30%–60% decrease in mean RMSE values is observed over the range of system delays tested. Both ANN structure and IW optimizations decrease prediction errors. Nevertheless, the comparison between cases 2 and 4 (more than 30% decrease), as well as cases 3 and 4 (10% decrease) show that ANN structure optimization performs a more important role in error reduction. Detailed results from each patient are plotted in Fig. 7.

TABLE III. Motion prediction results obtained with optimized ANN structure and IW for each patient.

| Patient | 2nd fraction RMSE (mm) | | | | | | 3rd fraction RMSE (mm) | | | | | |
|---------|------------------------|-----|-----|-----|-----|-----|------------------------|-----|-----|-----|-----|-----|
| | System delay (ms) | | | | | | System delay (ms) | | | | | |
| | 120 | 200 | 280 | 360 | 440 | 520 | 120 | 200 | 280 | 360 | 440 | 520 |
| 1 | 0.7 | 0.9 | 1.1 | 1.2 | 1.3 | 1.4 | 0.8 | 0.9 | 1.1 | 1.3 | 1.5 | 1.7 |
| 2 | 0.3 | 0.3 | 0.4 | 0.4 | 0.4 | 0.4 | 0.5 | 0.6 | 0.6 | 0.7 | 0.7 | 0.8 |
| 3 | 0.3 | 0.3 | 0.4 | 0.5 | 0.5 | 0.6 | 0.3 | 0.3 | 0.4 | 0.5 | 0.6 | 0.6 |
| 4 | 0.2 | 0.2 | 0.2 | 0.2 | 0.3 | 0.3 | 0.1 | 0.1 | 0.2 | 0.2 | 0.2 | 0.2 |
| 5 | 0.5 | 0.6 | 0.7 | 0.8 | 0.9 | 1.1 | 0.4 | 0.6 | 0.7 | 0.7 | 0.8 | 0.9 |
| 6 | 0.5 | 0.6 | 0.7 | 0.8 | 0.9 | 0.9 | 0.4 | 0.5 | 0.5 | 0.6 | 0.6 | 0.6 |
| 7 | 0.6 | 0.7 | 0.8 | 1.0 | 1.1 | 1.2 | 0.5 | 0.7 | 0.8 | 0.9 | 1.0 | 1.1 |
| 8 | 0.2 | 0.2 | 0.3 | 0.3 | 0.3 | 0.4 | 0.1 | 0.1 | 0.2 | 0.2 | 0.2 | 0.2 |
| 9 | 0.2 | 0.3 | 0.4 | 0.5 | 0.5 | 0.6 | 0.3 | 0.4 | 0.4 | 0.5 | 0.6 | 0.7 |
| 10 | 0.2 | 0.2 | 0.3 | 0.3 | 0.3 | 0.4 | 0.2 | 0.3 | 0.3 | 0.3 | 0.4 | 0.4 |
| 11 | 0.9 | 1.1 | 1.2 | 1.4 | 1.5 | 1.6 | 1.0 | 1.3 | 1.6 | 1.8 | 2.1 | 2.2 |
| 12 | 1.5 | 1.7 | 1.9 | 2.1 | 2.3 | 2.4 | 1.8 | 2.1 | 2.3 | 2.5 | 2.6 | 2.8 |
| 13 | 0.1 | 0.1 | 0.1 | 0.1 | 0.1 | 0.1 | 0.0 | 0.0 | 0.1 | 0.1 | 0.1 | 0.1 |
| 14 | 1.4 | 1.7 | 2.0 | 2.2 | 2.4 | 2.6 | 1.4 | 1.7 | 2.0 | 2.3 | 2.5 | 2.8 |
| 15 | 0.2 | 0.2 | 0.3 | 0.4 | 0.4 | 0.5 | 0.6 | 0.7 | 0.9 | 1.0 | 1.0 | 1.1 |
| 16 | 0.3 | 0.3 | 0.4 | 0.4 | 0.4 | 0.5 | 0.5 | 0.5 | 0.6 | 0.7 | 0.7 | 0.8 |
| 17 | 0.7 | 0.8 | 0.9 | 1.0 | 1.2 | 1.2 | 0.6 | 0.8 | 0.9 | 1.0 | 1.1 | 1.2 |
| 18 | 0.6 | 0.8 | 0.9 | 1.0 | 1.1 | 1.1 | 0.5 | 0.6 | 0.7 | 0.8 | 0.9 | 1.1 |
| 19 | 0.4 | 0.5 | 0.6 | 0.7 | 0.8 | 0.9 | 0.7 | 0.9 | 1.1 | 1.2 | 1.4 | 1.6 |
| 20 | 0.3 | 0.4 | 0.5 | 0.5 | 0.6 | 0.6 | 0.3 | 0.4 | 0.4 | 0.5 | 0.6 | 0.6 |
| 21 | 0.0 | 0.0 | 0.0 | 0.1 | 0.1 | 0.1 | 0.1 | 0.1 | 0.1 | 0.1 | 0.1 | 0.1 |
| 22 | 0.4 | 0.4 | 0.4 | 0.5 | 0.5 | 0.5 | 0.5 | 0.5 | 0.5 | 0.6 | 0.6 | 0.6 |
| 23 | 0.9 | 1.1 | 1.2 | 1.3 | 1.3 | 1.4 | 0.8 | 0.8 | 1.0 | 1.0 | 1.0 | 0.9 |
| 24 | 0.3 | 0.4 | 0.5 | 0.5 | 0.6 | 0.6 | 0.2 | 0.3 | 0.3 | 0.4 | 0.4 | 0.5 |
| 25 | 0.2 | 0.2 | 0.2 | 0.2 | 0.2 | 0.2 | 0.4 | 0.4 | 0.5 | 0.6 | 0.6 | 0.7 |
| 26 | 0.3 | 0.4 | 0.5 | 0.5 | 0.5 | 0.6 | 0.5 | 0.6 | 0.7 | 0.8 | 0.9 | 1.0 |
| 27 | 0.2 | 0.2 | 0.2 | 0.3 | 0.3 | 0.3 | 0.1 | 0.2 | 0.2 | 0.2 | 0.3 | 0.3 |
| 28 | 1.3 | 1.6 | 1.9 | 2.2 | 2.4 | 2.7 | 0.4 | 0.4 | 0.5 | 0.5 | 0.6 | 0.6 |
| 29 | 0.6 | 0.7 | 0.9 | 1.1 | 1.2 | 1.3 | 0.7 | 0.8 | 0.9 | 1.0 | 1.0 | 1.1 |
| Mean | 0.5 | 0.6 | 0.7 | 0.8 | 0.8 | 0.9 | 0.5 | 0.6 | 0.7 | 0.8 | 0.9 | 0.9 |

Figure 8 shows the prediction accuracy of the 3rd fraction data using two different sets of ANN structure as: (1) ANN structures optimized to predict 3rd fraction data, and (2) ANN structures optimized to predict 2nd fraction data. Smaller RMSE values are observed in several patients using the ANN structures specifically optimized to predict the 3rd fraction. However, the mean RMSE values from all patients are the same for all system delays in both cases (0.5–0.9 mm).

TABLE IV. Relative mean RMSE values comparison.

| Case | Relative mean RMSE (2nd fraction) | | | | | | Relative mean RMSE (3rd fraction) | | | | | |
|------|-----------------------------------|-----|-----|-----|-----|-----|-----------------------------------|-----|-----|-----|-----|-----|
| | System delay (ms) | | | | | | System delay (ms) | | | | | |
| | 120 | 200 | 280 | 360 | 440 | 520 | 120 | 200 | 280 | 360 | 440 | 520 |
| 1 | 0.4 | 0.5 | 0.5 | 0.6 | 0.6 | 0.7 | 0.5 | 0.5 | 0.6 | 0.6 | 0.7 | 0.7 |
| 2 | 0.5 | 0.6 | 0.6 | 0.6 | 0.7 | 0.7 | 0.5 | 0.6 | 0.6 | 0.6 | 0.7 | 0.7 |
| 3 | 0.9 | 0.9 | 0.9 | 0.9 | 0.9 | 0.9 | 0.9 | 0.9 | 0.9 | 0.9 | 0.9 | 0.9 |
| 4 | 1 | 1 | 1 | 1 | 1 | 1 | 1 | 1 | 1 | 1 | 1 | 1 |

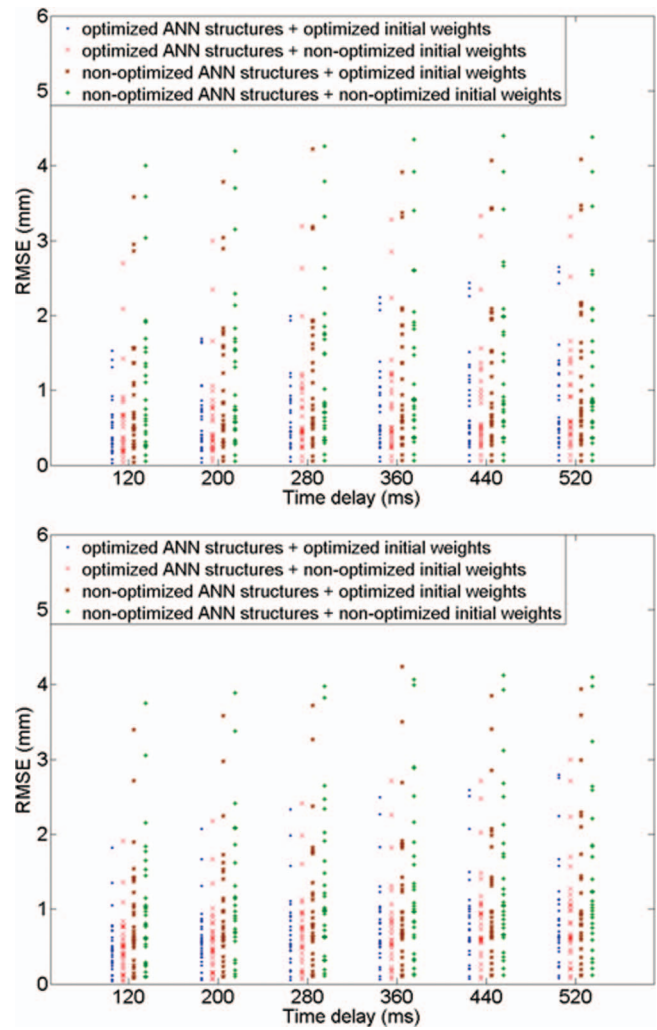


FIG. 7. Prediction accuracy comparisons in four different cases [(top) 2nd fraction prediction and (bottom) 3rd fraction prediction].

IV. DISCUSSION

Superior performance of ANN in respiratory motion prediction over other methods has been reported by comparative studies,^{13,28} and several studies have been conducted in surrogates-based tumor tracking systems.^{15,16} However, we believe this is the first study utilizing ANN for lung-tumor motion prediction in a MRI-based tracking environment.

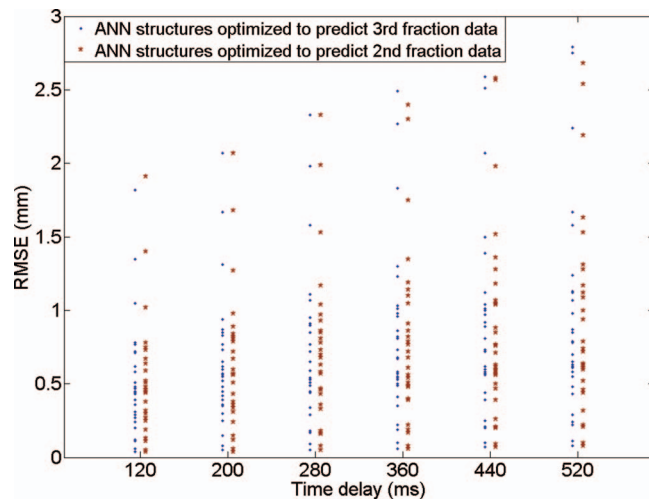


FIG. 8. Prediction accuracy of 3rd fraction data using (1) ANN structures optimized to predict 3rd fraction, and (2) ANN structures optimized to predict 2nd fraction

Real-time lung tumor tracking requires a MR imaging rate of 3–4 fps.²¹ Currently, this rate cannot be achieved in 3D real-time imaging. However, we proved that 2D real-time MR imaging is feasible at 3.6 fps in our previous study (Dynamic Scan Time = 275 ms, FOV: 40 cm × 40 cm, 3.1 mm × 3.1 mm × 20 mm).⁹ Using this, tumor motion data obtained from each MR image would generate good training data.

We have demonstrated the advantage of using multiple ANNs. The MR imaging rate is fixed at every 280 ms. The purpose of implementing multiple ANNs is to reduce the frequency of MLC failures during tumor tracking. The result shown in Table II clearly demonstrates the advantage of using seven ANNs over a single ANN. Using seven ANNs, MLC was always able to reach its set points, and the mean MLC-off time was decreased by a factor of more than 7.

Seven ANNs are chosen in this study to evaluate the accuracy of our predictor using the Suh *et al.*²² data. However, in a real case, a larger or smaller number of ANNs can be easily implemented in a given tracking system depending on the expected MR imaging rate and the frequency of MLC motion triggering.

The advantage of optimizing ANN structures and IW for each patient has been investigated. There is a 30%–60% decrease of mean RMSE values if ANN structure and IW are optimized, in comparison to motion prediction using a single ANN structure and randomly chosen IW. This was obtained using seven ANNs of an identical structure. Because each of these ANNs corresponds to a different amount of system delay, it may be possible to further improve the prediction accuracy if we optimize each ANN structure for its specific system delay. This will allow the ANN structure changes among the seven ANNs, which will be a subject of future studies.

The entire optimization process for each treatment fraction of a given patient takes ~2.5 h on the computer platform used, which would mandate calculations to be performed prior to treatment. Faster computers can, of course, be introduced for faster calculations.

The results shown in Fig. 8 suggest no significant advantage in prediction performance using fraction specific ANN structure optimization. This is based on the three consecutive fractions of motion data available in this study. However, further investigations are required with patient data obtained from a larger number of consecutive fractions.

As explained in Sec. II.H.1, after every 7th data point is chosen from the original tumor motion pattern, each motion pattern is shifted and normalized before it is presented to the ANN. This is clinically feasible as the characteristics of a given patient's lung-tumor motion, such as the maximum amplitude and mean position, can be observed just before the beam delivery through the 2.5 min training session as shown in Step 2 of Fig. 1. Thus, an appropriate amount of shifting and a proper normalization factor can be determined for each treatment fraction.

Moreover, this should be implemented as a safety feature for motion prediction using ANN, because the normalization factor can be used as an upper limit for future tumor positions. In our ANN design shown in Fig. 2, the output value must stay between 0 and 1. Therefore, the maximum future tumor position that can be predicted by our ANN is restricted by the normalization factor, even if the ANN starts to diverge during treatment.

This study is focused on predicting 1D lung-tumor motion in the SI direction. Lung-tumors may, however, move up to 15 mm in AP, and 10 mm in LR directions during normal breathings.^{4,5} Therefore, predicting future tumor positions in a realistic 3D space is an important issue in intrafractional MR tumor tracking. Extension of our predictor to this matter will be very straightforward and will be investigated in future studies.

V. CONCLUSION

A new ANN-based lung-tumor motion predictor is developed for MRI-based intrafractional tumor tracking. The MR imaging rate was fixed at 280 ms. The predictive performance of the predictor was evaluated in its ability to predict tumor positions in 40 ms intervals that corresponded to the acquisition rate of independent test patient data (acquired every 40 ms) obtained in Ref. 22.

Three practical issues of regarding ANN implementation in MRI-based lung-tumor tracking, (1) selecting proper ANN structures and IW, (2) reducing tracking failures, and (3) developing ANN training methods, are addressed in this study. The performance-accuracy of our predictor is evaluated with data from 29 lung cancer patients simulating clinically realistic situations.

Mean RMSE values of 0.5–0.9 mm (ranges 0.0–2.8 mm from 29 patients) are achieved by our predictor for system delays ranging from 120 to 520 ms. The advantage of using a patient specific ANN structure and IW optimizations is shown by the 30%–60% decrease in mean RMSE values in motion prediction as compared to results achieved with a single ANN structure and randomly chosen IW. Also, the results suggest no significant advantage in prediction performance from a fraction specific ANN structure optimization.

ACKNOWLEDGMENTS

The authors thank Dr. Paul Keall, Dr. Yelin Suh, and Dr. Sonja Dieterich from Stanford University for the lung-tumor motion data used for this study.

^aElectronic mail: Gino.Fallone@albertahealthservices.ca

- ¹M. B. Tacke, S. Nill, A. Krauss, and U. Oelfke, "Real-time tumor tracking: Automatic compensation of target motion using the Siemens 160 MLC," *Med. Phys.* **37**(2), 753–761 (2010).
- ²A. Sawant, R. L. Smith, R. B. Venkat, L. Santanam, B. C. Cho, P. Poulsen, H. Cattell, L. J. Newell, P. Parikh, and P. J. Keall, "Toward submillimeter accuracy in the management of intrafraction motion: The integration of real-time internal position monitoring and multileaf collimator target tracking," *Int. J. Radiat. Oncol., Biol., Phys.* **74**(2), 575–582 (2009).
- ³B. Cho, P. R. Poulsen, A. Sloutsky, A. Sawant, and P. J. Keall, "First demonstration of combined Kv/Mv image-guided real-time dynamic multileaf-collimator target tracking," *Int. J. Radiat. Oncol., Biol., Phys.* **74**(3), 859–867 (2009).
- ⁴H. Shirato, Y. Seppenwoolde, K. Kitamura, R. Onimura, and S. Shimizu, "Intrafractional tumor motion: Lung and liver," *Semin. Radiat. Oncol.* **14**(1), 10–18 (2004).
- ⁵C. Plathow, C. Fink, S. Ley, M. Puderbach, M. Eichinger, I. Zuna, A. Schmahl, and H. U. Kauczor, "Measurement of tumor diameter-dependent mobility of lung tumors by dynamic MRI," *Radiother. Oncol.* **73**(3), 349–354 (2004).
- ⁶A. Krauss, S. Nill, M. Tacke, and U. Oelfke, "Electromagnetic real-time tumor position monitoring and dynamic multileaf collimator tracking using a Siemens 160 MLC: Geometric and dosimetric accuracy of an integrated system," *Int. J. Radiat. Oncol., Biol., Phys.* **79**(2), 579–587 (2010).
- ⁷L. I. Cervino, J. Du, and S. B. Jiang, "MRI-guided tumor tracking in lung cancer radiotherapy," *Phys. Med. Biol.* **56**(13), 3773–3785 (2011).
- ⁸B. G. Fallone, B. Murray, S. Rathee, T. Stanescu, S. Steciw, S. Vidakovic, E. Blosser, and D. Tymofichuk, "First MR images obtained during megavoltage photon irradiation from a prototype integrated linac-MR system," *Med. Phys.* **36**(6), 2084–2088 (2009).
- ⁹J. Yun, E. Yip, K. Wachowicz, S. Rathee, M. Mackenzie, D. Robinson, and B. G. Fallone, "Evaluation of a lung tumor autocontouring algorithm for intrafractional tumor tracking using low-field MRI: A phantom study," *Med. Phys.* **39**(3), 1481–1494 (2012).
- ¹⁰J. Yun, M. MacKenzie, D. Robinson, S. Rathee, B. Murray, and B. G. Fallone, "Real-time MR tumour tracking using a Linac-MR system," in *Proceedings of the 56th Annual Meeting of the COMP*, Ottawa, ON, June 16–19, 2010.
- ¹¹H. Shirato, K. Suzuki, G. C. Sharp, K. Fujita, R. Onimaru, M. Fujino, N. Kato, Y. Osaka, R. Kinoshita, H. Taguchi, S. Onodera, and K. Miyasaka, "Speed and amplitude of lung tumor motion precisely detected in four-dimensional setup and in real-time tumor-tracking radiotherapy," *Int. J. Radiat. Oncol., Biol., Phys.* **64**(4), 1229–1236 (2006).
- ¹²G. C. Sharp, S. B. Jiang, S. Shimizu, and H. Shirato, "Prediction of respiratory tumour motion for real-time image-guided radiotherapy," *Phys. Med. Biol.* **49**(3), 425–440 (2004).
- ¹³A. Krauss, S. Nill, and U. Oelfke, "The comparative performance of four respiratory motion predictors for real-time tumour tracking," *Phys. Med. Biol.* **56**(16), 5303–5317 (2011).
- ¹⁴P. S. Verma, H. M. Wu, M. P. Langer, I. J. Das, and G. Sandison, "Survey: Real-time tumor motion prediction for image-guided radiation treatment," *Comput. Sci. Eng.* **13**(5), 24–35 (2011).
- ¹⁵J. H. Goodband, O. C. L. Haas, and J. A. Mills, "A comparison of neural network approaches for on-line prediction in IGRT," *Med. Phys.* **35**(3), 1113–1122 (2008).
- ¹⁶M. J. Murphy and D. Pokhrel, "Optimization of an adaptive neural network to predict breathing," *Med. Phys.* **36**(1), 40–47 (2009).
- ¹⁷H. R. Maier and G. C. Dandy, "The effect of internal parameters and geometry on the performance of back-propagation neural networks: An empirical study," *Environ. Modell. Software* **13**(2), 193–209 (1998).
- ¹⁸L. F. A. Wessels and E. Barnard, "Avoiding false local minima by proper initialization of connections," *IEEE Trans. Neural Networks* **3**(6), 899–905 (1992).
- ¹⁹C. Plathow, S. Ley, C. Fink, M. Puderbach, W. Hosch, A. Schmahl, J. Debus, and H. U. Kauczor, "Analysis of intrathoracic tumor mobility during whole breathing cycle by dynamic MRI," *Int. J. Radiat. Oncol., Biol., Phys.* **59**(4), 952–959 (2004).
- ²⁰P. Yen, R. W. Katzberg, M. H. Buonocore, and J. Sonico, "Dynamic MR imaging of the temporomandibular joint using a balanced steady-state free precession sequence at 3T," *Am. J. Neuroradiol.* 1–3 (2011).
- ²¹P. J. Keall, G. S. Mageras, J. M. Balter, R. S. Emery, K. M. Forster, S. B. Jiang, J. M. Kapatoes, D. A. Low, M. J. Murphy, B. R. Murray, C. R. Ramsey, M. B. Van Herk, S. S. Vedam, J. W. Wong, and E. Yorke, "The management of respiratory motion in radiation oncology report of AAPM Task Group 76," *Med. Phys.* **33**(10), 3874–3900 (2006).
- ²²Y. Suh, S. Dieterich, B. Cho, and P. J. Keall, "An analysis of thoracic and abdominal tumour motion for stereotactic body radiotherapy patients," *Phys. Med. Biol.* **53**(13), 3623–3640 (2008).
- ²³S. S. Haykin, *Neural Networks: A Comprehensive Foundation* (Prentice Hall, Englewood Cliffs, NJ, 1999).
- ²⁴L. Behera, S. Kumar, and A. Patnaik, "A novel learning algorithm for feed-forward networks using lyapunov function approach," in *Proceedings of International Conference on Intelligent Sensing and Information Processing*, IEEE, Chennai, India, Jan. 4–7, 2004, pp. 277–282.
- ²⁵J. Kennedy and R. Eberhart, "Particle swarm optimization," in *Proceedings of the 1995 IEEE International Conference on Neural Networks*, IEEE, Perth, Australia, Nov. 27–Dec. 1, 1995, pp. 1942–1948.
- ²⁶Y. H. Shi and R. Eberhart, "A modified particle swarm optimizer," in *Proceedings of the 1998 IEEE International Conference on Evolutionary Computation*, IEEE, Anchorage, Alaska, May 4–9, 1998, pp. 69–73.
- ²⁷Y. Tsunashima, T. Sakae, Y. Shioyama, K. Kagei, T. Terunuma, A. Nohomi, and Y. Akine, "Correlation between the respiratory waveform measured using a respiratory sensor and 3D tumor motion in gated radiotherapy," *Int. J. Radiat. Oncol., Biol., Phys.* **60**(3), 951–958 (2004).
- ²⁸M. J. Murphy and S. Dieterich, "Comparative performance of linear and nonlinear neural networks to predict irregular breathing," *Phys. Med. Biol.* **51**(22), 5903–5914 (2006).